AIAA JOURNAL
Vol. 38, No. 10, October 2000

Flow Properties of a Supersonic Turbulent Boundary Layer with Wall Roughness

Robert M. Latin*
Air Force Institute of Technology, Wright–Patterson Air Force Base, Ohio 45433-7765
and
Rodney D. W. Bowersox†
University of Alabama, Tuscaloosa, Alabama 35487-0280

An experimental study of the influence of surface roughness on the mean and turbulent flow properties of a high-speed ($M = 2.9$, $Re/\mathrm{m} = 2.0 \times 10^7$) turbulent boundary layer flow was performed. Six wall topologies, including a smooth and five rough surfaces consisting of three random sand-grain plates and two uniformly machined plates ($k_s^+ = 100$–570), were tested. Mean flow measurements included surveys of the velocity and density. Turbulence quantities included direct measurements of the kinematic velocity turbulence intensities, mass flux turbulence intensities, the kinematic Reynolds shear stress, the compressible Reynolds shear stress and the density-transverse-velocity fluctuation correlation. The trends in the mean flow, observed for incompressible flow, were found to hold for the present study when Van Driest II scaling was used. Kinematic statistical turbulent flow properties were found to scale by local mean quantities. Conversely, turbulent flow statistical properties with an explicit thermodynamic dependence did not scale by local mean quantities and had a strong linear dependence on roughness height. Roughness was found to extend the region where inner scaling held toward larger values of y^+ for the compressible Reynolds shear stress, the x- and y-velocity component turbulence intensities, the x-component of the mass flux turbulence intensity, and the density-transverse-velocity correlation.

Nomenclature

A_B = roughness frontal blockage area
B' = constant
C_f = skin friction coefficient
k = roughness height
k^+ = $\rho_w u^* k / \mu_w$
L = length scale
M = Mach number
p = pressure
Re = Reynolds number ($\rho_e u_e L / \mu_e$)
T = temperature
U = mean Favre axial velocity
u, v, w = velocity components
u^+ = u / u^*
u^* = friction velocity
x, y, z = Cartesian coordinates
y^+ = $\rho_w u^* y / \mu_w$
Δ = $(\,)_{\mathrm{rough}} - (\,)_{\mathrm{smooth}}$
Δx = length from nozzle exit to the measurement location
Δx_0 = effective starting length due to finite thickness of the boundary layer at $x = 0$
δ = boundary-layer thickness ($u / u_e = 0.99$)
δ_M = boundary-layer thickness ($M / M_e = 0.99$)
δ^* = displacement thickness
δ^+ = $\rho_w u^* \delta / \mu_w$
θ = momentum thickness
λ = roughness wavelength
ρ = density
τ = shear stress

Subscripts

e = boundary-layer edge condition
i = $x = 0$
k = kinematic
s = equivalent sand-grain roughness
t = total condition
w = wall
0 = smooth plate

Superscripts

T = turbulent
$'$ = Reynolds fluctuation
$-$ = Reynolds mean component
$''$ = Favre fluctuation

Introduction

SUPERSONIC boundary layers are responsible for skin friction drag and convection heat transfer over high-speed aircraft, missiles, reentry vehicles, and propulsion systems. Surface roughness increases these engineering quantities and enhances transition from laminar to turbulent flow. Since all manufactured components of these systems have some inherent surface roughness or become rough through operation, it is important to quantify how surface roughness affects supersonic boundary layers in both a qualitative and quantitative manner to enable better understanding and prediction methods.

Direct numerical simulation of high-Reynolds-number turbulent flow is currently impractical. Hence, engineers and scientists must rely on an approximate averaged form of the governing Navier–Stokes equations. Because of the nonlinearity of the Navier–Stokes equations, averaging introduces additional unknowns into the problem. Modeling these additional turbulence unknowns has proven to be a major challenge and a key limiting factor in the accuracy of

Table 1 Measurement flow conditions

Measurement	P_t, Pa	T_t, K	Re/m ($\times 10^{-7}$)
Pitot	$2.17 \times 10^5 \pm 0.4\%$	296 ± 1.0	1.9 ± 0.3
Cross-film (x–y plane)	$2.22 \times 10^5 \pm 0.3\%$	293 ± 1.0	2.0 ± 0.3
Cross-film (x–z plane)	$2.39 \times 10^5 \pm 0.3\%$	296 ± 1.0	2.1 ± 0.3
Laser Doppler	$2.41 \times 10^5 \pm 0.5\%$	294 ± 1.0	2.1 ± 0.3
Color schlieren	$2.17 \times 10^5 \pm 0.4\%$	296 ± 1.0	1.9 ± 0.3

Received 10 March 1999; revision received 8 March 2000; accepted for publication 31 March 2000. This material is declared a work of the U.S. Government and is not subject to copyright protection in the United States.

*Graduate Research Assistant, Department of Aeronautics and Astronautics. Member AIAA.

†Assistant Professor, Department of Aerospace Engineering and Mechanics. Senior Member AIAA.

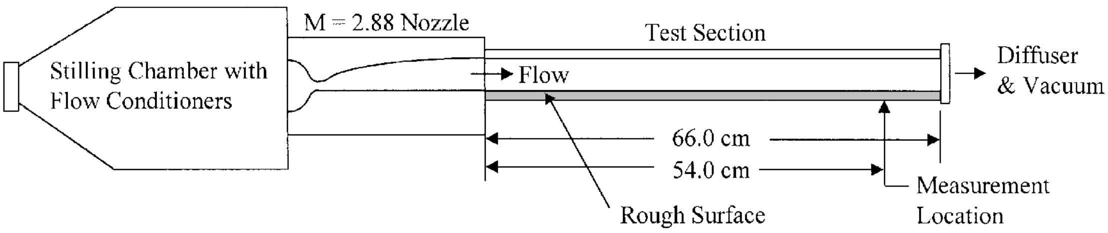

Fig. 1 Schematic of wind tunnel (not drawn to scale).

Table 2 Surface conditions

Model	$\bar{k}$, mm	$\sqrt{\overline{k'^2}}$,[a] mm	$k_{\max}$,[a] mm	T_w,[b] K	ρ_w,[b] kg/m^3	k_s,[c] mm	k_s^+[c]	A_B, mm^2
Flat	0.007	0.005	0.02	276	0.11	0.00	0	0.0
Two-dimensional	0.56	0.007	0.58	274	0.12	1.09	289	35.6
Three-dimensional	0.56	0.007	0.58	273	0.12	0.91	241	9.1
80 Grit	0.53	0.17	1.10	273	0.12	0.44	104	33.7
36 Grit	0.90	0.34	1.40	273	0.12	1.42	395	57.2
20 Grit	0.83	0.50	1.70	273	0.12	1.98	571	52.7

[a] For the two-dimensional and three-dimensional plates, the standard deviation was taken as $\frac{1}{3}$ the machining accuracy (22.4 μm).
[b] Adiabatic wall temperature ($T_t = 295$ K, $P_t = 2.22$ kPa, Mach number given in Table 1).
[c] $k_s = 0$ by definition ($k^+ \approx 1.1$).

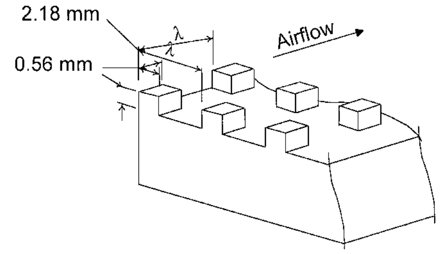

Three-dimensional plate

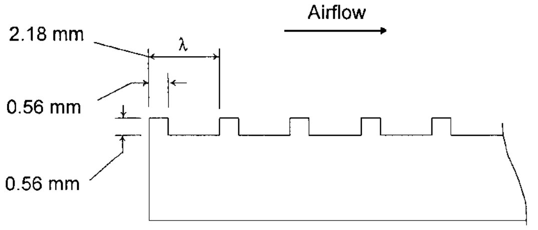

Two-dimensional plate

Fig. 2 Machined roughness patterns.

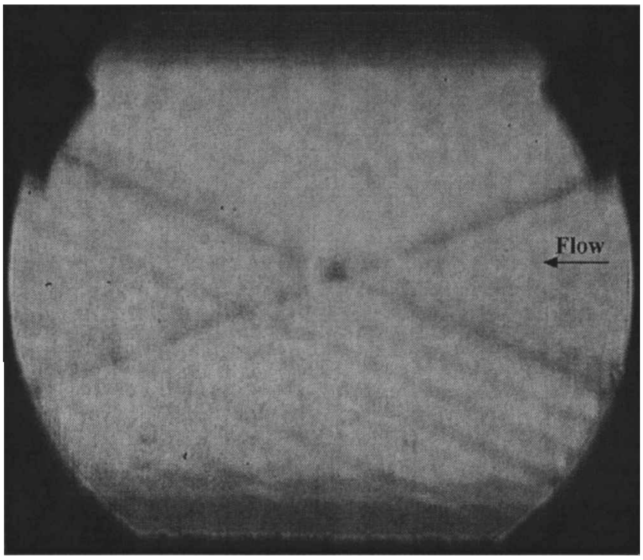

Fig. 3 Horizontal knife edge schlieren photograph (rough surfaces along the bottom): 20 Grit sandpaper plate.

Table 3 Measurement uncertainty

Measurement		Uncertainty	
x, y, mm		0.25, 0.13	
δ_i, δ, mm		1.0, 2.5	
δ^*, mm		0.08	
θ_i, θ, mm		0.04, 0.02	
$C_{f,0}$, $C_f(\times 10^{-4})$		1.0, 2.0	
$M_e(\times 10^{-2})$[b]		1.4	
y/δ[a] $\Rightarrow$	0.2	0.5	1.0
$\bar{u}/u_e(\times 10^{-2})$[b]	1.3	1.0	0.8
$\bar{u}/u_e(\times 10^{-2})$[c]	1.3	1.4	1.2
$\sqrt{(\overline{u'^2})}/\bar{u}(\times 10^{-3})$	2.1	1.9	1.5
$\sqrt{\overline{v'^2}}/\bar{u}(\times 10^{-3})$	0.8	1.1	1.1
$\overline{u'v'}/\bar{u}^2(\times 10^{-4})$	0.7	2.9	0.4
$\overline{\rho u}/\rho_e u_e(\times 10^{-2})$	2.9	3.3	3.6
$\sqrt{\overline{(\rho u)'^2}}/\overline{\rho u}(\times 10^{-3})$	6.0	7.0	2.0
$\sqrt{\overline{(\rho v)'^2}}/\overline{\rho u}(\times 10^{-3})$	5.0	4.0	3.0
$\sqrt{\overline{(\rho w)'^2}}/\overline{\rho u}(\times 10^{-3})$	5.0	3.5	2.5
$\overline{(\rho u)'(\rho v)'}/\overline{\rho u^2}(\times 10^{-4})$	4.2	4.3	1.1
$\overline{(\rho u)'(\rho w)'}/\overline{\rho u^2}(\times 10^{-4})$	4.2	4.3	1.1
$\bar{\rho}/\rho_e(\times 10^{-2})$	3.2	3.6	3.8
$\overline{\rho' v'}/\bar{\rho}\bar{u}(\times 10^{-4})$	4.3	5.2	1.2

[a] Errors in units plotted (based on smooth-plate results).
[b] Pitot probe.
[c] Laser Doppler velocimetry.

high-Reynolds-number numerical simulations. Empirical information is a key element in understanding the essential dynamics and has thus provided the basis for current turbulence models for both low- and high-speed flows.[1–3]

For low-speed rough-wall flow, the influence of surface roughness on the mean and turbulent flow properties is well documented,[1,4–8] and the associated flow scaling[1] has provided the foundation for turbulence models suitable for low-speed zero-pressure-gradient rough-wall flow.[2] From the experimental descriptions, surface roughness has been shown to have a direct influence on the inner region of the law of the wall and is typically described by a single parameter, namely, the roughness Reynolds number k^+. Nikuradse[4] demonstrated that sand-grain-generated roughness increased the velocity defect and skin friction and shifted the logarithmic region of the law of the wall downward. The amount of downward shift was shown to be a function of k^+. Schlichting[1] introduced the concept of equivalent sand-grain roughness k_s^+ to correlate any surface roughness to the equivalent Nikuradse sand-grain roughness for comparison. Because the equivalent sand-grain roughness does not include roughness geometry or spacing, investigations of the influence of the roughness geometry were also performed.[5–7]

The available rough-wall database for high-speed flow is not as complete as that for low-speed. For example, rough-wall studies that included turbulence were not included in recent compilations of available mean and turbulent flowfield information.[3,9] However, the mean flowfield properties have been thoroughly documented.[10–12] Goddard[10] presented a detailed investigated the influence of Mach number ($M = 0.7$–4.54) on the mean velocity and skin friction for sand-grain surface roughness ($k_s^+ \approx 10$–1500) boundary-layer flow over a body of revolution. The Reynolds number range, depending on the Mach number, was nominally $Re_x \approx 2 \times 10^6$–$1 \times 10^7$. Goddard found that the shift in the law of the wall velocity profile was a function of k_s^+ and followed the same law as the incompressible case when the Van Driest II[13] compressibility transformation was used. Berg[11] extended the Mach number range to 6.0.

Liepmann and Goddard[14] conjectured that for fully rough flow, the wall shear force is primarily the result of the drag on the roughness elements. Based on this argument, they showed that the ratio of compressible to incompressible skin friction is equal to the wall-to-freestream density ratio. The force-balance data of Goddard[10]

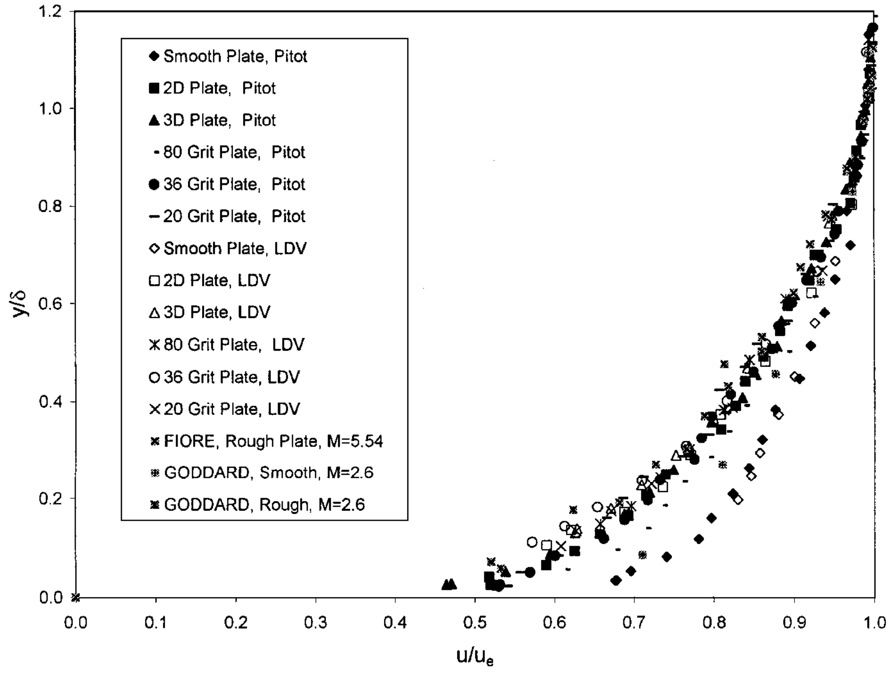

a) Mean velocity profiles (LDA and pitot data)

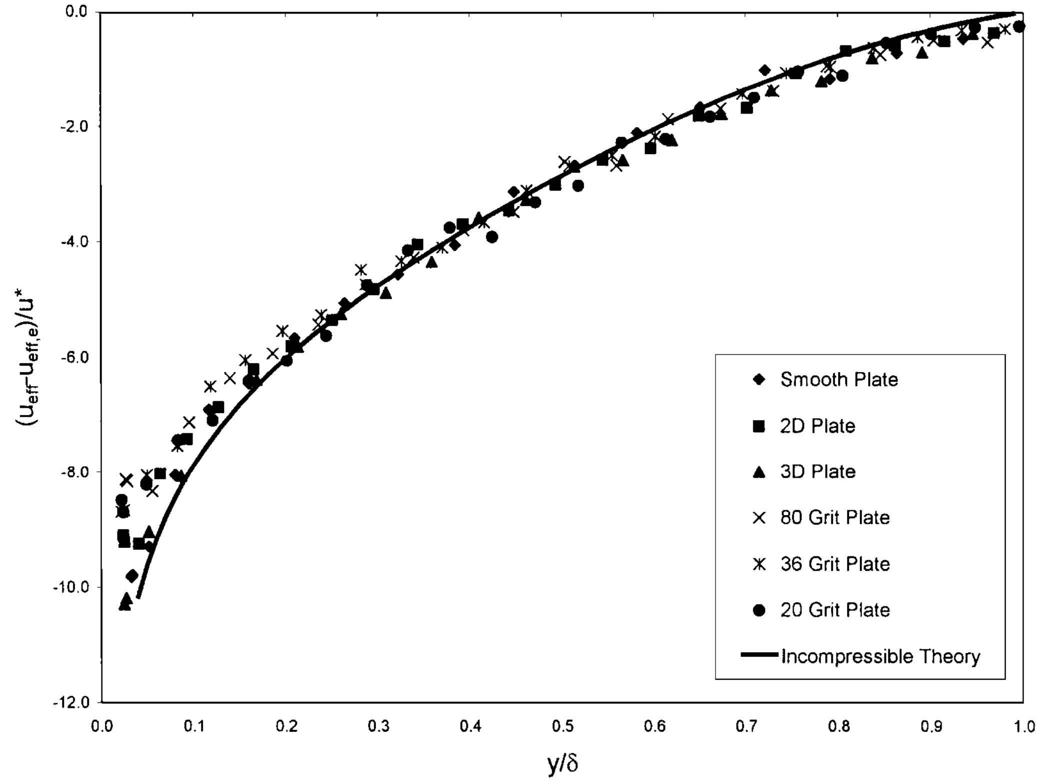

b) Effective velocity defect (pitot data)

Fig. 4 Mean flow profile data.

Table 4 Reference values ($x = 54$ cm)

Model	M_e	δ, mm	δ_M, mm	δ^*, mm	θ, mm	B'	C_f	u^*, m/s	Δx_0, cm	Re_x ($\times 10^7$)	Re_θ ($\times 10^4$)
Flat	2.75	12.4	15.4	3.32	0.80	N/A	0.00159	26	27.5	1.6 ± 0.8	1.6
Two-dimensional	2.73	16.8	18.1	5.82	1.32	21.4	0.00363	38	7.9	1.2 ± 0.6	2.6
Three-dimensional	2.73	15.8	17.3	5.67	1.29	21.8	0.00353	38	8.1	1.2 ± 0.6	2.6
80 Grit	2.73	14.7	16.3	4.77	1.11	23.9	0.00302	35	9.2	1.2 ± 0.6	2.2
36 Grit	2.72	18.0	19.2	6.24	1.43	21.4	0.00393	40	8.0	1.2 ± 0.6	2.9
20 Grit	2.70	17.7	18.2	6.26	1.45	21.0	0.00399	40	7.7	1.2 ± 0.6	2.9

[a] Defined such that $u/u_e = 0.99$. [b] Defined such that $M/M_e = 0.99$.

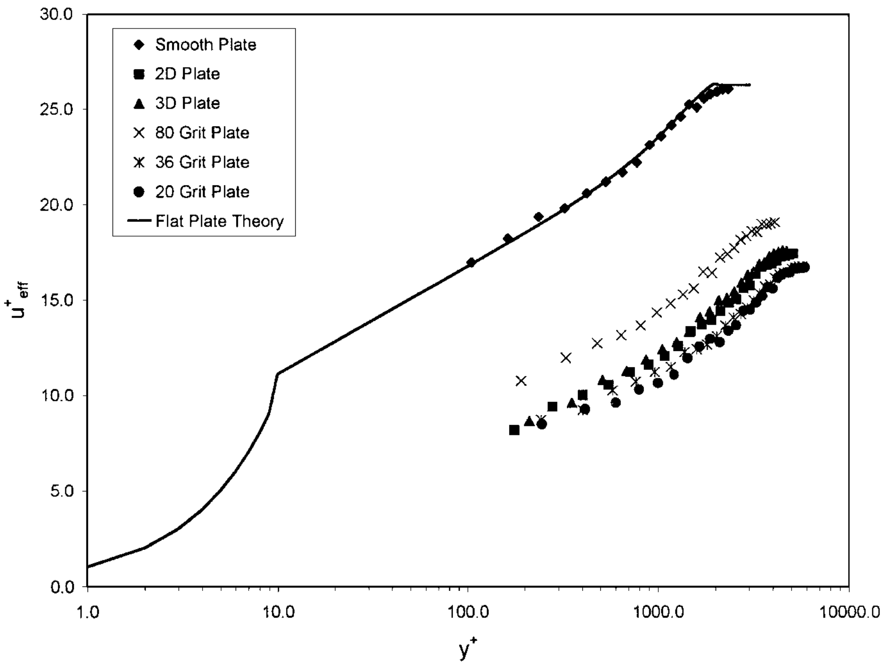

c) Effective law of the wall plot (pitot data)

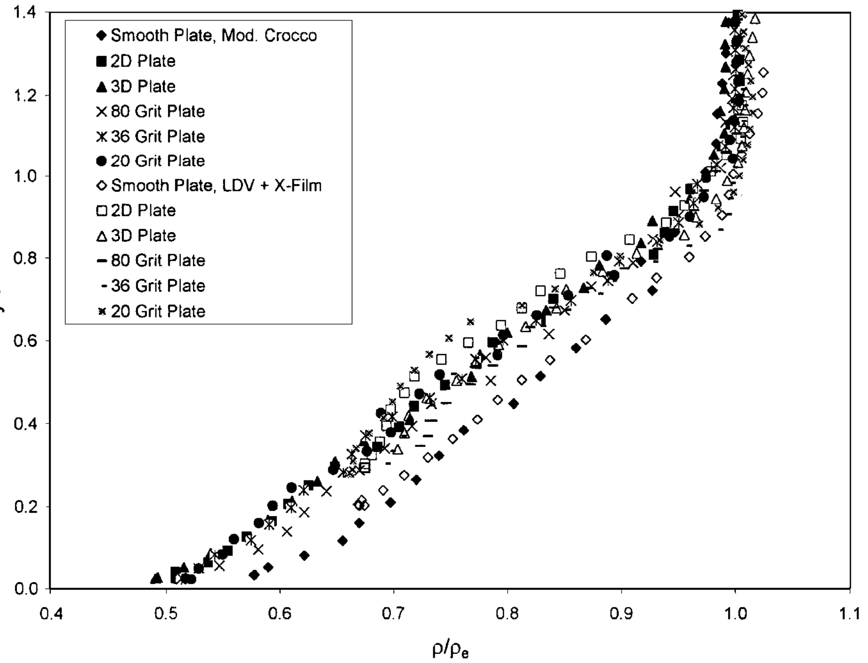

d) Density (modified Crocco and combined LDA and cross film)

Fig. 4 Mean flow profile data (continued).

confirmed the Liepmann and Goddard skin friction correlation over a Mach number range of 0.7–4.54. The available skin friction data[10–12] are well correlated (nominal variance of ±15%) for $k_s^+ \in [10, 1500]$, $M \in [0.7, 6.0]$, as

$$C_f / C_{f,0} = 0.39 \ln\left(k_s^+\right) + 0.103 \qquad (1)$$

As first observed by Morkovin,[15] it appears that many of the differences in the turbulent statistical properties across supersonic and subsonic smooth-plate boundary layers can be explained, or at least correlated, by the thermodynamic property variations across the layer. This observation, termed Morkovin's hypothesis, has provided the rationale for using incompressible turbulence models for flows up to Mach 5. Scaling for compressibility has been found to correlate the mean velocity with the low-speed database across smooth and rough boundary layers.[10,13] More recently, detailed compilations and analyses of available high-speed turbulence smooth-wall data[3,9,16–18] were performed. In summary, the studies indicated that the database was insufficient to confirm turbulent property scaling and that the realm of applicability of Morkovin's hypothesis might be more restrictive than originally believed.[3,9,16–18]

Supersonic flows often possess features that do not have incompressible counterparts. For example, supersonic flow over rough surfaces can generate shock and expansion waves that interact with boundary-layer turbulence. This interaction is especially true at those higher Mach numbers where most of the boundary layer is supersonic. For a flat plate at Mach 3.0, approximately 99% of the boundary layer is supersonic. Hence, the presence of relatively small roughness elements could generate significant compressibility effects.

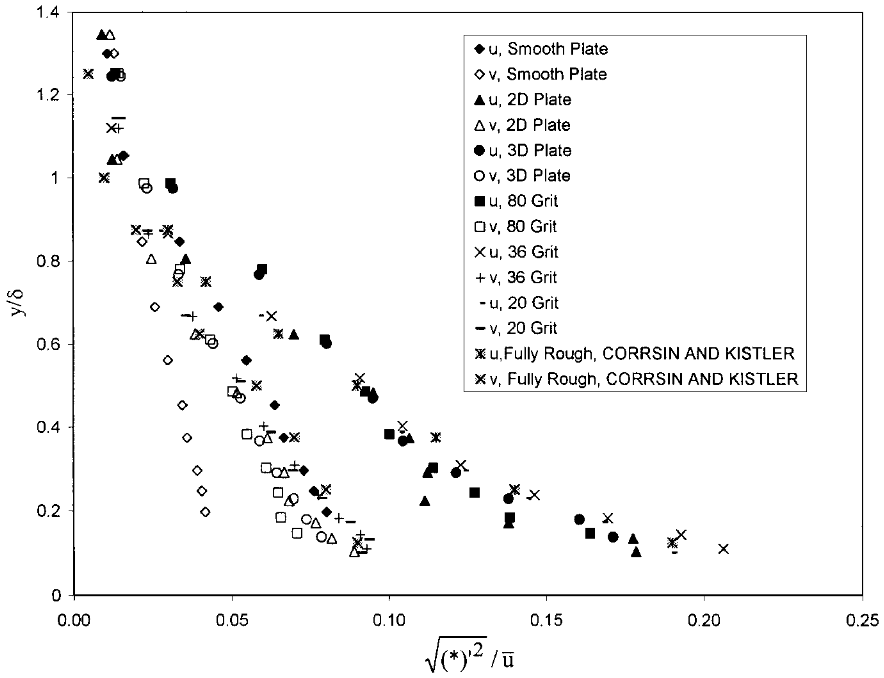

a) Outer variable scaling

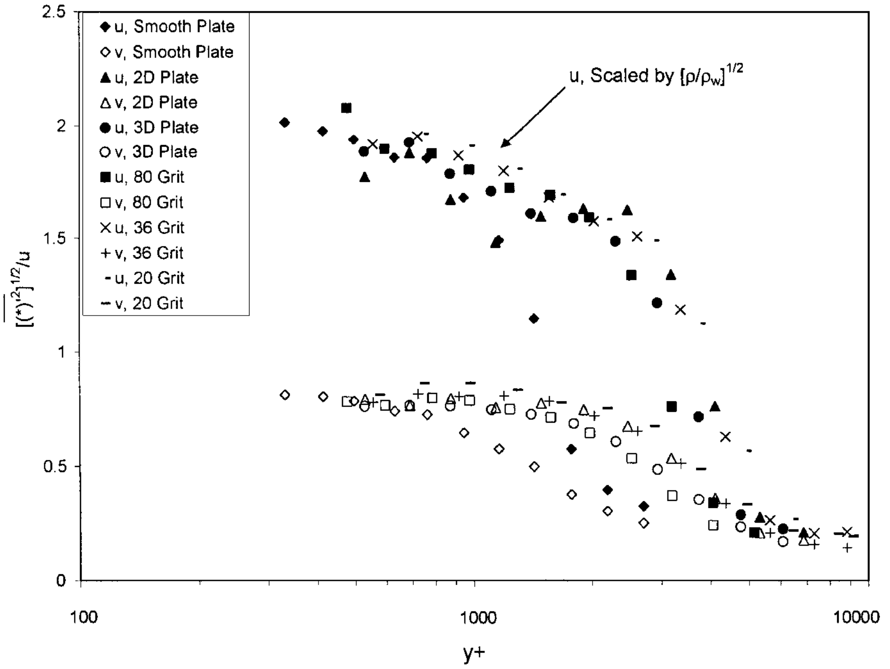

b) Inner variable scaling

Fig. 5 *u*- and *v*-turbulence intensity profiles.

The objective of the present study was to provide an experimental characterization of the influence of roughness ($k_s^+ = 100$–570) on the mean and turbulent flow properties across a supersonic high-Reynolds-number turbulent boundary-layer flow. Six wind-tunnel wall models, consisting of a smooth plate (for comparison purposes), two uniformly distributed rough surfaces, and three sand-grain rough surfaces, were examined. All of the rough surfaces were in the fully regime rough.[1] Detailed surveys of the mean velocity, mean density, kinematic velocity turbulence intensities, mass flux turbulence intensities, kinematic Reynolds shear stress, compressible Reynolds shear stress, and the density-transverse-vebcity fluctuation correlation across the rough-wall boundary layers were acquired. In addition, an investigation of empirical scaling for the mean and turbulent flow properties was performed.

Experimental Apparatus

Facilities

Data were collected in a supersonic wind tunnel located at Wright–Patterson Air Force Base. The tunnel was a combination drawdown/blowdown facility. A 27.46-cm-long (measured from the throat), finite-radius half nozzle was used to produce a freestream Mach number at the nozzle exit of 2.88 with a ±1.3% variation across the test section.[19−22] The contoured side of the nozzle was located along the tunnel ceiling. The average axial velocity freestream turbulence intensity at the nozzle exit, measured with a cross-film probe, was nominally 0.8% (Refs. 19–22). The stagnation flow conditions for each measurement technique are listed in Table 1. The boundary-layer heights δ, δ_M, and θ at the nozzle exit were calculated from the velocity profile measured with the pitot probe (described in Experimental Apparatus: Instrumentation) as 4.7, 5.3, and 0.2 mm, respectively. The cross-sectional shape of the test section was square, with each side 6.35 cm in length. For the present study, the test section length, beginning at the nozzle exit, was 66.0 cm, with the measurement location at 54.0 cm downstream of the nozzle exit (Fig. 1). The coordinate system was defined such that x was positive in the freestream flow direction, measured from the nozzle exit; y was positive vertically up relative to the tunnel floor; z completed the right-hand system, and $z = 0$ was along the tunnel span centerline.

Detailed two-dimensionality studies quantifying the mean and turbulent flow statistics at off-center z locations have been performed for the present facility.[19−22] In summary, the mean flow properties were independent of z location to within the measurement uncertainty over the center 40% of the test section (total area mapped).[19] The turbulent shears stresses at off centerline locations also agreed to within the measurement uncertainty[20] (total area mapped was about 20% of the test section). The effects of the longitudinal pressure gradient due to boundary-layer growth were also investigated,[21,22] and the results demonstrated that the mean and turbulent flow properties measured at x locations (in the present coordinate system with the origin at the test section exit) of 16.5, 44.0, and 54.0 cm (present location) collapsed onto a single curve representative of a zero-pressure-gradient equilibrium boundary layer with outer scaling.

Six different floor sections were tested, each section having a different surface roughness. As was the case for the Goddard[10] study, the floor sections were aligned so that the tops of the roughness elements were level with the tunnel floor at the nozzle exit (Fig. 1).

Three sand-grain roughened plates were constructed by adhering Varathane brand 80, 36, and 20 Grit flooring sandpaper to the top surface of three aluminum flat plates (66.0 × 6.35 × 1.91 cm^3). The heights of the sand grains were not measured prior to being glued to the sandpaper surface. For this reason, the roughness heights of the sandpaper were not expected to correspond directly to Nikuradse sand-grain roughness. Instead, direct measurements of the roughness topography were made using a Carl Zeiss LSM 320 Confocal Laser Scan Microscope (LSM). The LSM was used to provide samples of the roughness topology from which the mean, maximum, and standard deviation of the surface roughness were computed. The roughness topologies were resolved with the LSM to within 4.0% of the mean roughness height. The statistical properties from this analysis are listed in Table 2. The 20 Grit plate was more sparsely populated with larger elements than the 36 Grit paper. Therefore, the average roughness height was smaller for the 20 Grit plate. However, the maximum height and the standard deviation were the largest for the 20 Grit plate. These three rough surfaces were selected because they provided a relatively broad (200%) variation in the maximum heights, and all were in the fully rough regime.

Two uniformly machined plates were designed to provide insight into the effects of topology. The geometry was arbitrarily chosen to provide a large variation in the frontal blockage (opposing the flow) and the surface area occupied by roughness elements. The machined two-dimensional roughness element model had rectangular lateral grooves that spanned the width of the test section, and the three-dimensional model consisted of cubical pillars (Fig. 2) aligned in straight rows in both the x and z directions. The wavelength of the roughness elements was 2.18 mm. The roughness

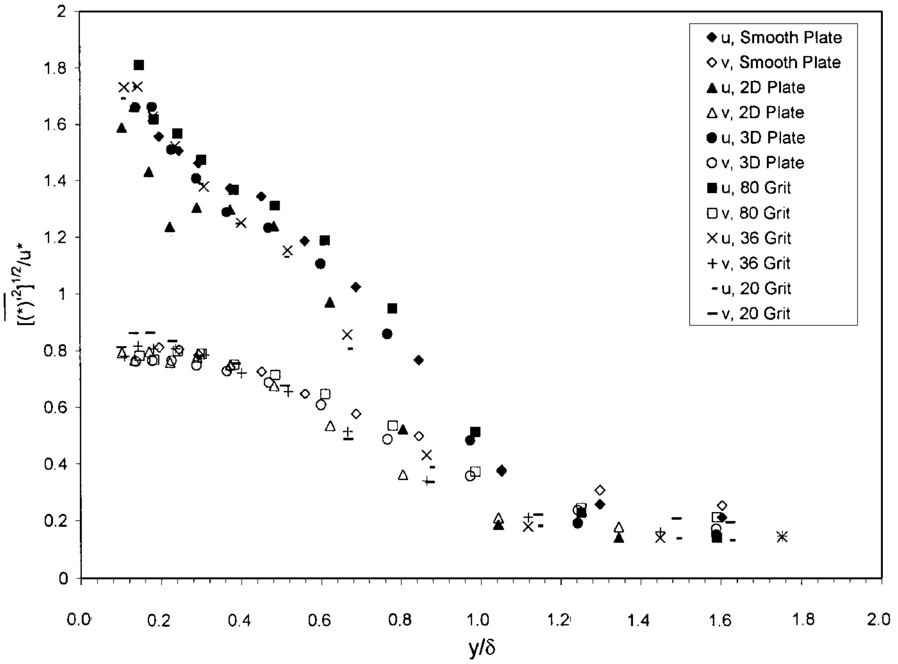

c) Mixed variable scaling

Fig. 5 *u*- and *v*-turbulence intensity profiles (continued).

height was chosen as 0.56 mm for both the two-dimensional and three-dimensional plates so that both were fully rough. The frontal blockage area for the two-dimensional plate was the roughness height times the width of the test section, which was 290% larger than that of the three-dimensional plate. The roughness blockage area A_B for each plate is summarized in Table 2. The surface area occupied by the two-dimensional plate (25.7%) was 290% larger than that for the three-dimensional plate (6.6%). The milling machine accuracy was rated at ±22 μm (±4.0% of the roughness element height).

Instrumentation

The color schlieren flow visualization equipment consisted of a mercury light source, two 15.24-cm parabolic mirrors (focal length of 1.97 m), a color slide (red–green–blue), and a Kodak Digital 460C CCD camera. Time-averaged (0.125-s) color schlieren photographs were acquired at the nozzle exit and test location (54.0 cm downstream of the nozzle exit).[19]

A pitot pressure probe was used to measure pressures across the boundary layers for the six models. The pitot probe was constructed from 1.59-mm-diam stainless steel tubing. The end of the probe was crimped such that the inner cross-section had a height of 0.8 mm and a width of 1.2 mm. Data were sampled at a rate of 800 Hz, and averages were computed over 200 samples. The Rayleigh–pitot formula was used to compute the Mach number from the measured pitot pressure. The usual compressible flow relations for thermally and calorically perfect air, with the assumption of an adiabatic flow in the mean, were used to calculate the velocity.

A DANTEC brand 57N Enhanced laser Doppler velocimetry system was used. The use of this laser Doppler velocimetry system in the present facility is documented in Ref. 23. A TSI brand six-jet atomizer was used to produce olive oil seed particles. The mean particle size was 0.6 μm. Thus, the mean 3-dB frequency response was 200 kHz, and the associated Stokes number was 0.06. Each data point in a given laser Doppler velocimetry profile represents a separate tunnel run. During a given run, data were collected for

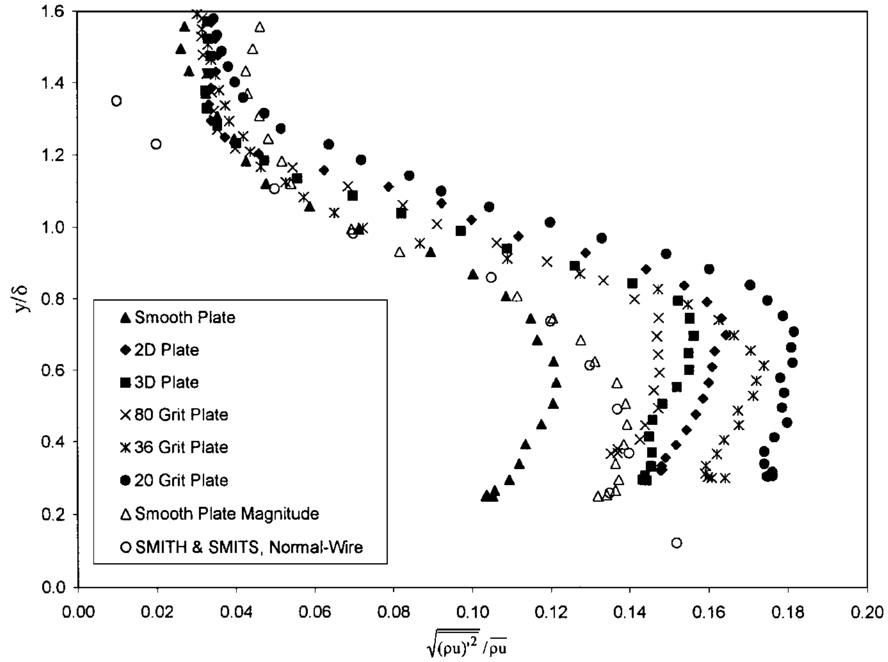

a) Outer-variable scaling

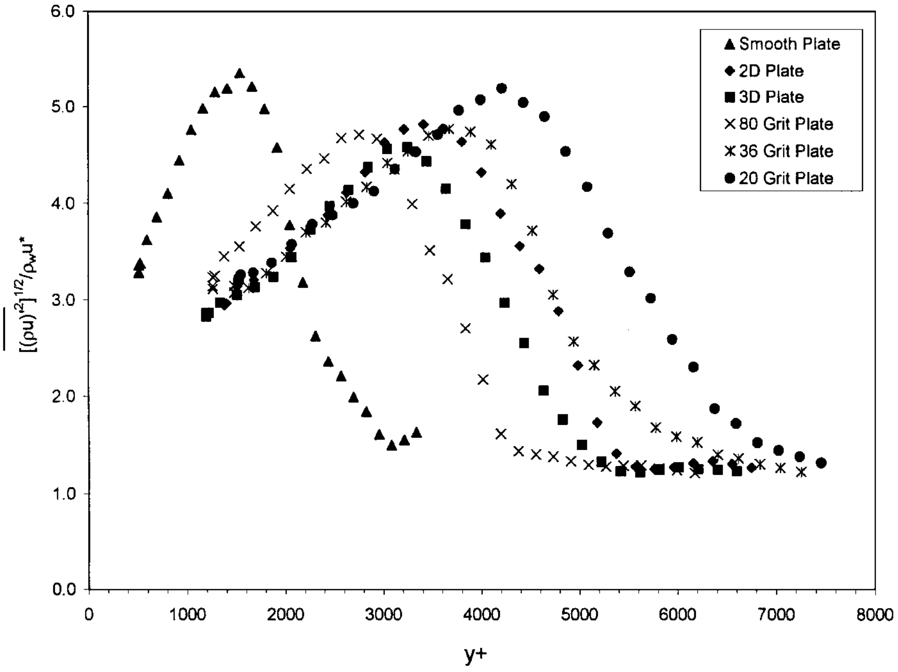

b) Inner-variable scaling

Fig. 6 ρu**-turbulence intensity profiles.**

a period of 12 s after the tunnel had reached steady state. Average data rates varied across the boundary layer but were generally in the range of 0.5–2.5 kHz.

A DANTEC brand StreamLine Constant Temperature Anemometry System was used for the cross-film anemometry measurements. TSI Model 1243/AN-20 cross-film probes were used to measure mean and turbulent information in the x–y and x–z planes. The probe sensors were cylindrical with a diameter of 50.8 μm and a length of 1.02 mm. The sensor separation was 1.09 mm. The frequency response of the cross-film probes was nominally 150 kHz, the data were sampled at a rate of 30 kHz, and statistical averages were computed over blocks of 3000 samples. The present cross-film results were found to be in excellent agreement with hot-wire measurements of Smith and Smits[24] (discussed in Results and Discussion: Turbulence Measurements). The probes were calibrated at angles very close to those found in the wind tunnel; therefore, heat conduction effects to the probe supports were implicitly included in the calibration. Since the boundary-layer flows here were essentially adiabatic in the mean,[19] single-overheat cross-film anemometry was used,[23] where the resistance ratio was set to 2.0 to minimize the total temperature sensitivity. Limited multiple-overheat data were acquired for the two-dimensional machined plate, and the measured total temperature fluctuation turbulence intensity levels were less than 3.3% (Ref. 19).

The combined laser Doppler velocimetry and cross-film anemometry data reduction procedures described in Ref. 23 were used in the present study. The compressible Reynolds shear stress for thin layer flow (i.e., $\bar{v}/\bar{u} \ll 1$) is related to the cross-film output, to second order, by the following relation[23]:

$$\frac{\tau^R_{xy}}{\bar{\rho}\bar{u}^2} \cong -\frac{\overline{u'v'}}{\bar{u}^2} - \frac{\overline{\rho'v'}}{\bar{\rho}\bar{u}} \cong -\frac{\overline{(\rho u)'(\rho v)'}}{(\overline{\rho u})^2} \qquad (2)$$

The first two terms on the right-hand side represents the full compressible Reynolds shear stress, and the last term was directly measured with the cross-film. The Favre averaged shear stress is equivalent to the kinematic shear stress [first term on the right-hand side of Eq. (2)] to the fourth order[23]; hence, the Favre averaged shear stress was directly measured with laser Doppler velocimetry.

The smooth-plate skin friction was measured with the floating element skin friction sensor. A detailed description of the gauge and the operating procedure is given in Ref. 25.

Measurement Uncertainties

A standard uncertainty analysis,[26] accounting for probe location, transducer calibration, and repeatability, was performed for the conventional pressure and temperature probe data. The uncertainties in the tunnel stagnation conditions are listed in Table 1. The position uncertainty was taken as 25% of the smallest division on the measurement standard. The smooth-plate floating element skin friction errors have been previously documented.[25] The rough-wall skin friction uncertainty was evaluated by perturbing the inputs (θ_i, θ, and Δx) by the uncertainties listed in Table 3. The uncertainty analysis of the laser Doppler velocimetry data accounted for probe volume location, record length, velocity gradient broadening,[27,28] laser beam angular alignment, seed bias,[28] density bias, coincidence filtering, and repeatability. The uncertainty estimate procedures are outlined in Luker et al.[22] The primary sources of uncertainty accounted for in the cross-film data were linearization, calibration, probe position, probe volume, and repeatability. The uncertainties in the profile data varied across the boundary layers. Hence, the values at three boundary-layer locations are listed in Table 3.

Results and Discussion

Flow Visualization

A sample color schlieren photograph centered on $x = 4.3$ cm (near the beginning of the roughened floor) for the 20 Grit model is presented in Fig. 3 (shown in grayscale). The rough surface was along the lower wall, and the flow was from the right. At this location, shock and expansion waves were generated by the individual roughness elements protruding into the supersonic portion of the boundary layer for all but the two-dimensional machined plate (the two-dimensional machined plate is discussed in the next paragraph). The location of the sonic line at the nozzle exit was estimated from the theoretical velocity profile (with Van Driest II scaling) as 0.07 mm. Thus, at the nozzle exit, all of the roughness elements protruded deeply into the supersonic region (see Table 2 for the maximum roughness heights) of the boundary layer. The strength and intensity of the waves increased as the roughness height increased. These roughness generated waves distorted the boundary-layer edge and were clearly visible in the freestream.

The two-dimensional plate had a λ/k ratio of 3.9, which ratio is referred to as a "d-type" roughness.[7,8] Perry et al.[7] remarked that, for a d-type rough wall, "the outer flow rides relatively undisturbed

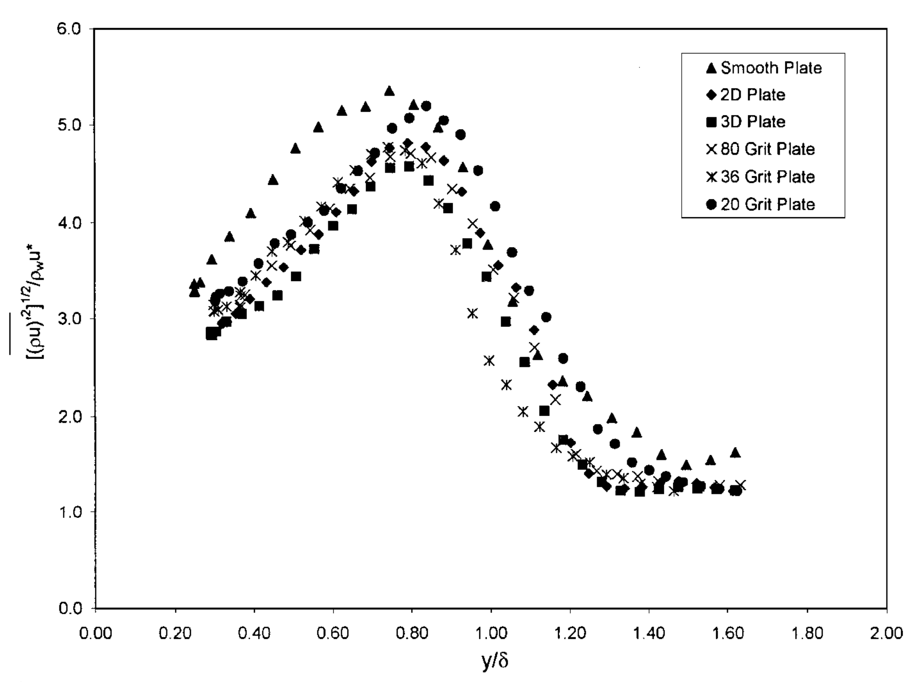

c) Mixed-variable scaling

Fig. 6 ρu-turbulence intensity profiles (continued).

over the crests of the elements." Hence, the lack of waves was not surprising.

At the measurement location ($x = 54.0$ cm), roughness-generated waves were not visible. The Mach number measurements at $y/\delta \approx 0.03$ (relative to the tops of the roughness elements) were ≤ 1.0 for all but the 80 Grit plate, where the measurement was 1.2. Hence for all but the 80 Grit plate, the roughness elements did not extend into the supersonic portion of the boundary layer at measurement location; it is also unlikely that the 80 Grit elements protruded significantly into the supersonic flow.

Noticeable in Fig. 3 is a nozzle exit and test section seam interface wave and a wave emanating from the nozzle exit upper surface. The angles of the waves were measured as approximately 21.0 deg, which is close to the Mach angle (20.3 deg); thus, these waves were very weak, and the disturbances were undetectable with the present laser Doppler velocimetry instrumentation.

Mean Flow Measurements

The velocity profiles for each of the six models measured with the laser Doppler velocimetry system and estimated from the pitot pressure profiles at the test location are shown in Fig. 4a. All velocity profiles are presented with the local velocity and boundary-layer height nondimensionalized by the model specific freestream velocity (u_e) and boundary-layer thickness (δ), respectively. Measured reference values at the test location are summarized in Table 4. The freestream velocities measured using the two methods were in excellent agreement (average difference of 0.3%). The data from Goddard[10] and Fiore (as shown in Ref. 29) agreed reasonably well

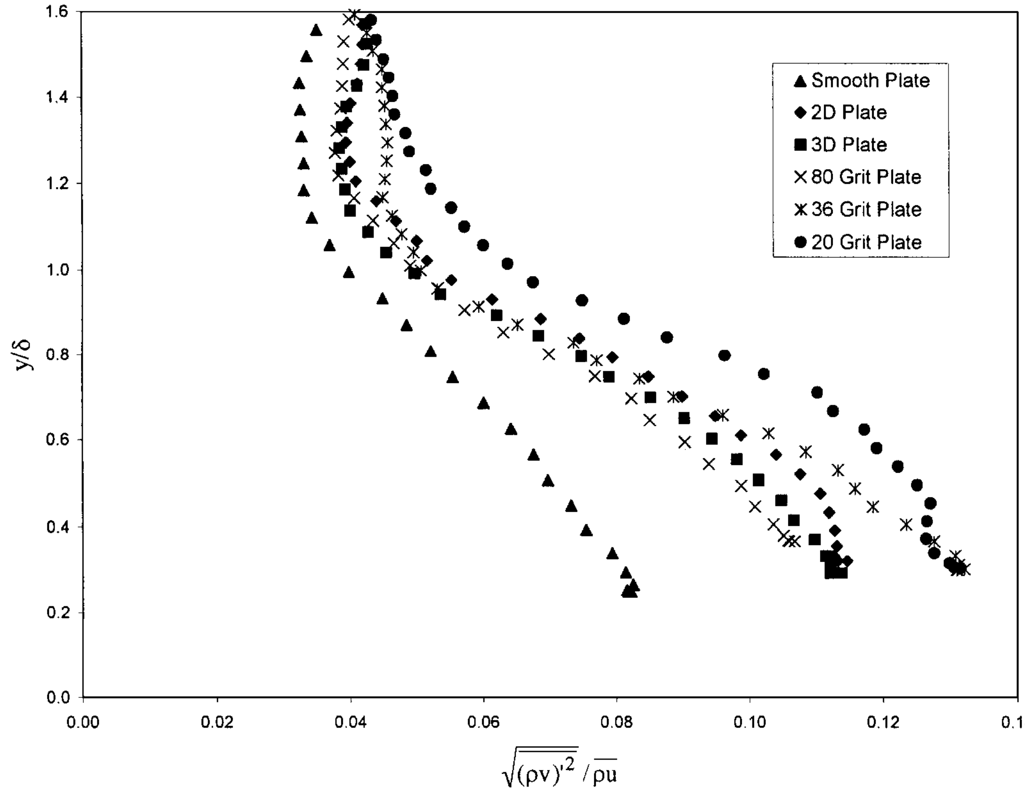

Fig. 7 ρv-turbulence intensity profiles (outer-variable scaling).

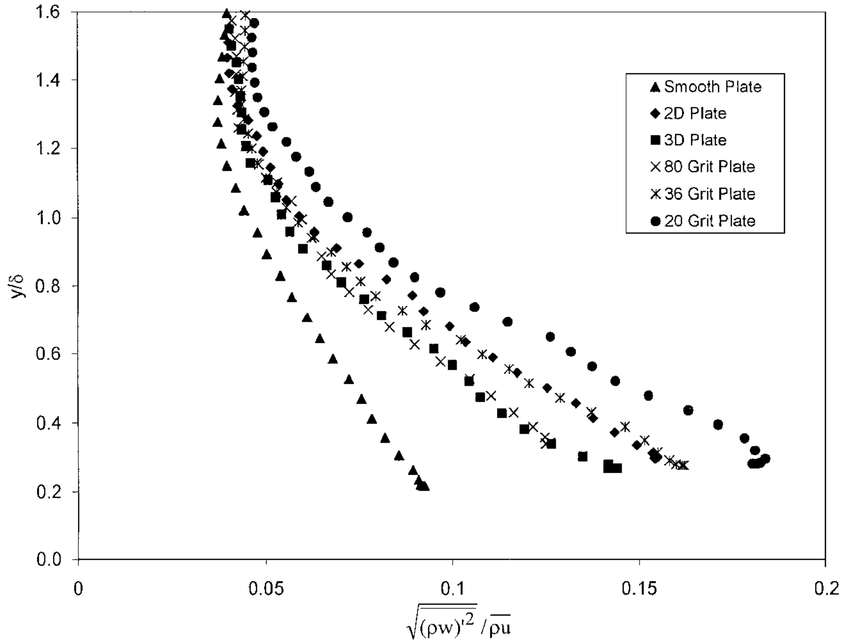

Fig. 8 ρw-turbulence intensity profiles (outer-variable scaling).

with the present experiments, and the slight differences were attributed to Reynolds number differences and errors in reading data from Goddard's figures. The 80 Grit pitot data indicated a slightly smaller defect than the other rough plates, which smallness indicated that the 80 Grit plate for the pitot data ($k_s^+ = 100$) was in the transitional roughness regime. The remaining fully rough velocity profiles in Fig. 4a all collapsed reasonably well onto a single curve.

The integral boundary-layer heights[30] were estimated from the velocity profile, where the density profile was estimated from the Modified Crocco Integral[30] (discussed later in this section). The integral boundary layer heights along with Re_θ are listed in Table 4. The proper Reynolds number to characterize the state of the boundary layer has been defined as $Re_{\theta_2} \equiv (\rho_e u_e \theta / \mu_w)$ (Refs. 9 and 18). For the present study, $Re_\theta / Re_{\theta_2} \approx 2.2$. Hence, the present study is in the medium-Reynolds-number category.[18]

The skin friction coefficient $C_{f,0}$ for the smooth plate was measured with a floating element skin friction gauge. In addition, $C_{f,0}$ was estimated using the Van Driest II skin friction relationship,[8] assuming that the flow could be modeled as a flat plate with the origin at the nozzle throat. The direct measurement and the Van Driest estimate agreed to within 1.0%. This excellent agreement was unexpected since the skin friction measurement uncertainty was estimated as nominally 6.0% (Ref. 25), and the accuracy of the Van Driest correlation is generally accepted to be 10% (Ref. 31).

The rough plate skin friction values were calculated using the fully rough law of the wall evaluated at the boundary layer edge[30]; specifically,

$$\sqrt{2/C_f} = 1/\kappa \ln(\delta/k) + B \tag{3}$$

where k is the roughness height, $\kappa = 0.41$, and B is a constant. Rewriting this equation using the momentum thickness and assuming that θ/δ was constant, gave $\sqrt{(2/C_f)} = 1/\kappa \ln(\theta/k) + B'$. Combining the equation with the zero pressure gradient momentum integral equation given by $C_f/2 = \mathrm{d}\theta/\mathrm{d}x$ and integrating gave

$$\left\{\frac{1}{\kappa^2}\frac{\theta}{k}\left[\ln^2\frac{\theta}{k} - 2\left(\ln\frac{\theta}{k} - 1\right)\right] + \frac{2B'}{\kappa}\frac{\theta}{k}\left(\ln\frac{\theta}{k} - 1\right) + B'^2\frac{\theta}{k}\right\}\Bigg|_{\theta_i/k}^{\theta_f/k} = \frac{\Delta x}{k} \tag{4}$$

With known values θ_i, θ_f, k, and Δx, the constant B' was calculated with Eq. (4) for each plate, and the corresponding skin friction coefficient was found from the law of the wall formula listed in Eq. (3). The values for θ_f (θ at $x = 54.0$ cm) for each plate are summarized in Table 4; $\Delta x = 54$ cm and k are mean values summarized in the first column of Table 1; and θ_i was the momentum thickness at the nozzle exit (listed earlier in Experimental Apparatus: Facilities). The skin friction values, along with B' from this analysis, are listed in Table 4. The present skin friction estimates agreed with Eq. (1) to within 3.0%.

Because the turbulent boundary layer was of finite thickness at the beginning of the rough surface, an effective length (Δx_0) of the rough surface was calculated using Eq. (4) by integrating from $\theta = 0$ to θ_i. The resulting effective starting lengths are listed in Table 4. For the smooth plate, the length of the wind tunnel nozzle was assumed. The resulting Reynolds numbers based on x ($x = \Delta x_0 + \Delta x$) are also listed in Table 4; the variances account for the stagnation condition variations listed in Table 2.

Figure 4b shows the defect law, with the Van Driest II compressibility transformation, for all six plate. By scaling the velocity defect with the friction velocity, all of the models collapse onto a single curve. Figure 4b also includes the correlation[30,32,33]

$$\frac{u_{\text{eff}} - u_{e,\text{eff}}}{u^*} = -\frac{1}{\kappa}\ln\left(\frac{y}{\delta}\right) + \frac{2\Pi}{\kappa}\left[1 - \sin^2\left(\frac{\pi}{2}\frac{y}{\delta}\right)\right] \tag{5}$$

where Π was estimated following White[32] as $0.8(\beta + 0.5)^{3/4} \approx 0.475$ and $\kappa = 0.41$. The agreement between the incompressible theory [Eq. 5] and the data was considered excellent. The main differences between the theory and the data are attributed to the determination of the boundary layer thickness. Based on the previously reported success of the Van Driest II scaling[13] and the collapsing of low-speed smooth and rough-wall defect law data,[30] the observed collapsing of the present data with Van Driest II scaling was the expected result.

The law of the wall plot with Van Driest II scaling is shown in Fig. 4c. The law of the wall,[30,32,33] given by

$$u_{\text{eff}}^+ = \begin{cases} y^+, & y^+ < 10 \\ \dfrac{1}{\kappa}\ln y^+ + 5.5 + \dfrac{2\Pi}{\kappa}\sin^2\left(\dfrac{\pi}{2}\dfrac{y}{\delta}\right), & y^+ \geq 10 \end{cases} \tag{6}$$

is also shown, where again $\Pi \approx 0.475$. As expected, the smooth plate data with Van Driest scaling[8] are in excellent agreement with the accepted theory. The equivalent sand-grain roughness heights

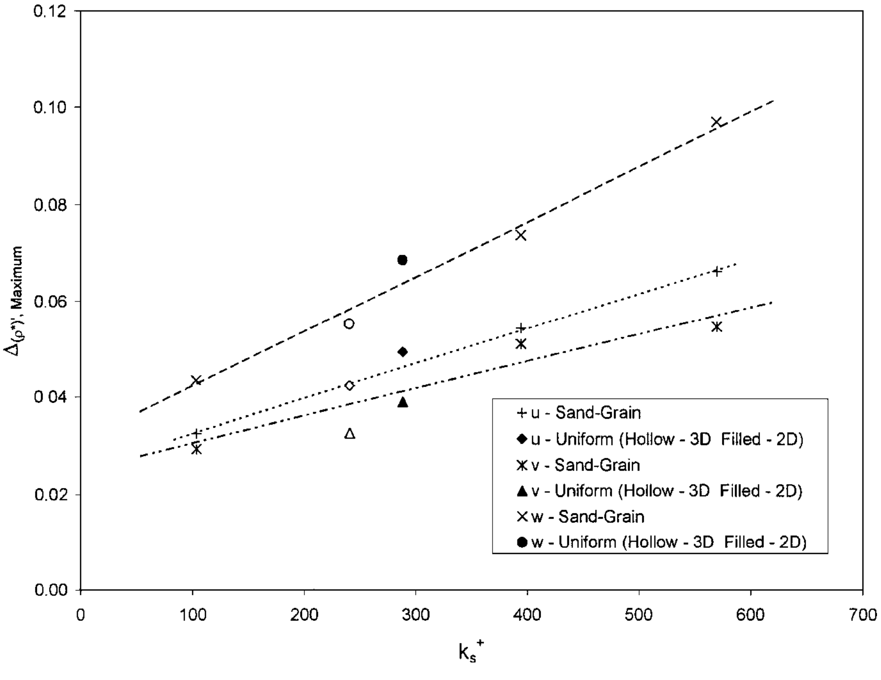

Fig. 9 Mass flux turbulence intensities vs k_s^+ (outer-variable-scaling).

(k_s) were calculated from the velocity profiles and the skin friction data as outlined in Refs. 1 and 6. The resulting k_s and k_s^+ values are listed in Table 2.

The density profile measurements for each of the six models, acquired with cross-film and laser Doppler velocimetry systems (i.e., $\bar{\rho} \cong \overline{\rho u}/\bar{u}$), are compared with the Modified Crocco Integral[30] estimate, obtained from the mean velocity measured with the pitot probe, in Fig. 4d. The agreement (10%) between the two methods for the smooth plate was considered good. The differences for the rough-wall plates were larger but were within the measurement uncertainty listed in Table 3.

Turbulence Measurements

The velocity turbulence intensities measured using the laser Doppler velocimetry system for all six models are shown in Fig. 5. Focusing first on the outer scaling plot (Fig. 5a), it was found that the rough plate u- and v-component turbulence intensity profiles collapsed when scaled by the local u-component of the mean velocity and boundary-layer height. The rough-plate turbulence intensities (both components) were approximately twice the smooth-plate values, with the largest, rough-wall u-component velocity turbulence intensity at 18.0 vs 9.0% for the smooth-plate case. For the v-component turbulence intensity, the largest rough plate value was approximately 9.0 vs 4.0% for the smooth-plate case. The incompressible rough-wall results from Corrsin and Kistler[8] are shown for comparison purposes. As indicated, their data agree very well with the present measurements considering the large differences in flow conditions. Compressibility scaling[15] was omitted so that only directly measured data are presented in Fig. 5a.

The present turbulence data were mostly in the outer region. However, plotting with inner variable scaling did produce discernable trends in the rough wall data. Shown in Fig. 5b are the turbulence

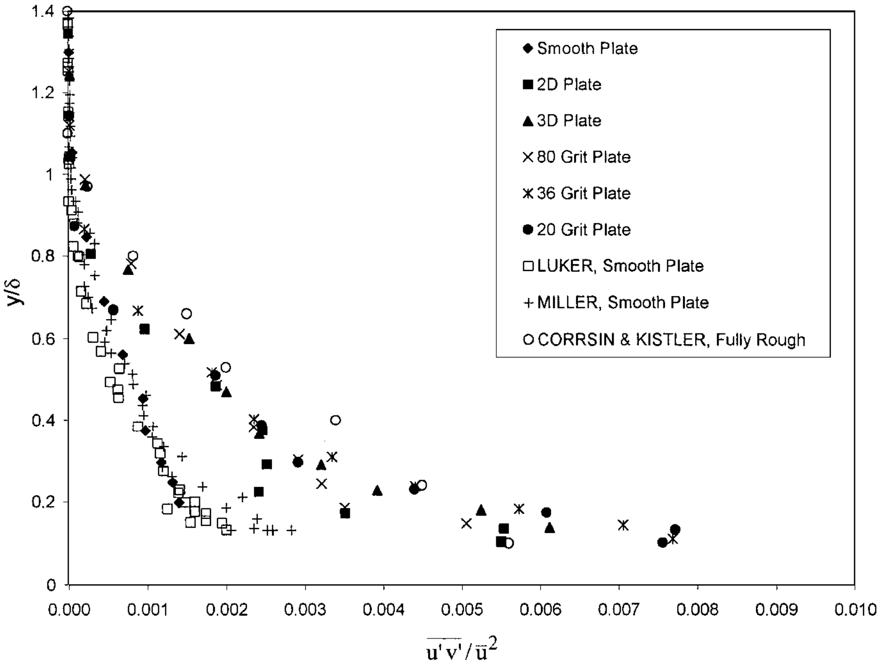

a) Outer-variable scaling

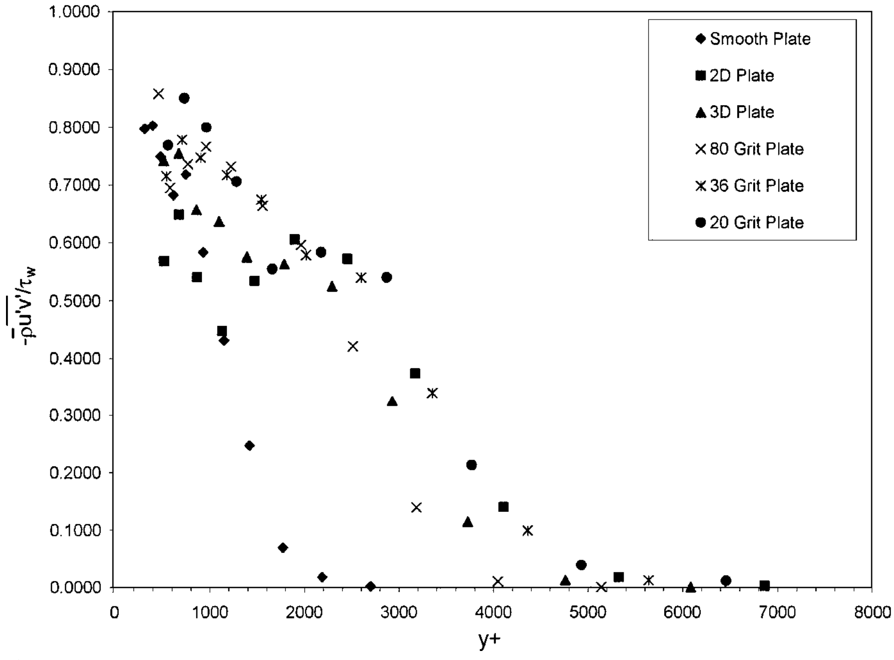

b) Inner-variable scaling

Fig. 10 Kinematic turbulent shear stress profiles.

intensity results normalized by the friction velocity plotted vs y^+. The smooth-plate levels shown in Fig. 5b are consistent with the incompressible data of Klebanoff[34] and the Mach 2.3 data of Elena and LaCharme,[35] as shown in Ref. 9. The rough-wall axial data merged with the smooth-wall data as the wall was approached when scaled for compressibility (as shown). Conversely, the transverse rough-wall fluctuations merged with the smooth-wall data as the wall was approached when plotted without the compressibility transformation (as shown).

Both the u- and v-component turbulence intensity profiles with mixed scaling (i.e., inner variable scaled turbulence intensity vs y/δ) are shown in Fig. 5c. The curves collapsed very well for $y/\delta < 0.6$. The only exception was the axial results for the two-dimensional machined plate (discussed in the next paragraph). Farther out into the boundary layer, the curves diverged and a discernible trend with roughness Reynolds number was observed. For both components, increasing the roughness shifted the curves vertically down on Fig. 5c.

The two-dimensional machined plate turbulence intensities (as shown in Figs. 5a–5c) did not collapse as well near the wall ($y/\delta < 0.4$). As discussed, the two-dimensional plate was also the only plate that did not produce shock and expansion waves. Hence, the two-dimensional plate turbulence production mechanisms in the inner region, which were most likely driven by cavity flow dynamics,[7,36] were fundamentally different than that of the other plates, where the roughness elements were all three dimensional.

The ρu-component turbulence intensity profiles measured with the cross-film probes are shown in Fig. 6. The profiles with outer variable scaling are given in Fig. 6a. Smooth-wall normal-wire Mach 2.9 boundary-layer data from Smith and Smits[24] are included in Fig. 6a for comparison purposes. Smith and Smits based their boundary-layer thickness δ on a total pressure ratio criterion of 98%, which was approximately equal to δ_M in the present study. Hence, the Smith and Smits y/δ values included in Fig. 6a were rescaled to the present definition (99% of u_e) by multiplying by δ_M/δ. Because normal-wire probes respond to the magnitude of the mass flux vector, the magnitude of the present cross-film results $\sqrt{[\overline{(\rho u)'^2} + \overline{(\rho v)'^2}]}$ is plotted for comparison. In the boundary layer, the present cross-film results (open triangles) are in very good agreement (to within the measurement uncertainties listed in Table 3) with the normal-wire data (open circles). In the free stream, the present results are higher than those of Smith and Smits[24]; these discrepancies were attributed to both facility differences and sensor resolution.

From an examination of the rough-wall data plotted in Fig. 6a, it was apparent that the mass flux turbulence intensity did not scale by the local mean flow as was the case for the u- and v-component turbulence intensities measured by laser Doppler velocimetry (Fig. 5a). Instead, a systematic increase with increasing roughness Reynolds number was observed. The mass flux turbulence intensities for each of the six models reached a maximum for y/δ in the range of 0.6–0.8. The relative increase with roughness is discussed the next paragraph. The cross-film freestream ρu turbulence intensity levels were 3–4%, with the value increasing slightly with increasing equivalent roughness height. It was expected that the shock and expansion waves that were generated by the roughness elements (Fig. 3) created slight increases in the freestream density fluctuations.

The ρu-component turbulence intensities scaled by the wall density and the friction velocity as a function of y^+ are shown in Fig. 6b. Presented in Fig. 6c are the ρu-component turbulence intensities scaled by the wall density and the friction velocity as a function of y/δ. In the region $y^+ \approx 500$–1300 in Fig. 6b for the smooth plate, the mass flux turbulence intensity increased to a distinct peak at $y^+ \approx 1600$. From Fig. 6c, the corresponding region was bounded by $y/\delta \approx 0.25$–0.6, and the peak was located at $y/\delta \approx 0.75$. Following the peak, the turbulence levels dropped off to the freestream values. The rough-wall data (Figs. 6b and 6c) followed a similar trend as the smooth-wall data. In Fig. 6b, curves were shifted toward higher values of y^+. In the region bounded by $y^+ \approx 1000$–3500 (Fig. 6b) or $y/\delta \approx 0.3$–0.8 (Fig. 6c), the rough-plate data were seen to collapse (the 80 Grit plate in Fig. 6b is the exception and is discussed in the next paragraph) onto almost a single linear curve. The rate of increase of the rough-wall curves in the region closest to the wall was significantly lower that that for the smooth plate in Fig. 6b, where the level of reduction of the slope, depended on the scaling, was approximately 30% (Fig. 6b) and 70% (Fig. 6c). The peak turbulence intensity level and the location of the peak in terms of y^+ (Fig. 6b) increased with the increasing roughness Reynolds number. In Fig. 6c, the peak values for the rough walls were nearly collocated at $y/\delta = 0.8$; the largest roughness element plate peak was slightly further out into the boundary layer ($y/\delta = 0.84$). The smooth-plate peak was clearly the largest, which coupled with the increasing peak value of the roughness Reynolds number, indicated that the wall shear stress increased more than the turbulence levels for the smaller roughness heights, and as the roughness height increased, the relative production of turbulence by the roughness increased.

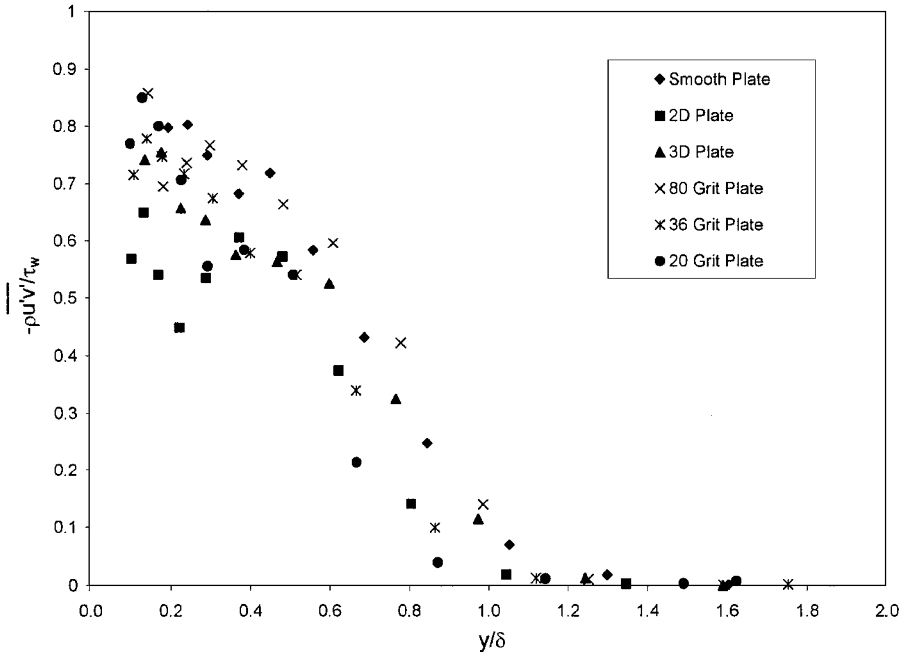

c) Mixed-variable scaling

Fig. 10 Kinematic turbulent shear stress profiles (continued).

In Fig. 6b, the 80 Grit data did not collapse onto the rough-wall curve for $y^+ \approx 1000$–3500. Recall that the velocity profile obtained with the pitot probe indicated that the 80 Grit plate data were in the transitional regime, and the cross-film data appear to have confirmed that conclusion. Hence, it is expected that a family of transitionally rough curves span the space between the smooth and fully rough plate limits. Interestingly, the kinematic velocity and turbulence data did not indicate that the 80 Grit plate was transitional. Two possible explanations for this apparent discrepancy are given. First, the 10% higher Reynolds number for the laser Doppler velocimetry data, as compared with the pitot and cross-film tests, might have been sufficient to shift the curve. Second, the inherent thermodynamic sensitivity of the cross-film and pitot probes might indicate that the boundaries of the roughness regimes depend on compressibility.

The ρv and ρw turbulence intensity profiles did not collapse when scaled with outer or inner variables. The effects of roughness on the turbulence levels are apparent in the results (outer scaling) plotted in Figs. 7 and 8. The maximums for both ρv- and ρw-components were located at the lowest point in the profile.

The peak ρu-, ρv-, and ρw-component turbulence intensity differences relative to the smooth-plate peak, $\Delta_{(\rho^*)'}$, from Figs. 6a, 7 and 8 are plotted vs the roughness Reynolds number in Fig. 9. The sand-grain roughness mass flux turbulence intensity difference data points fit reasonably well with a line, indicating that increasing the roughness height increased the mass flux turbulence intensity almost linearly. The ρw-turbulence intensity difference had the largest rate of increase (the slope of the linear fit was 1.1×10^{-4}). The ρu-turbulence intensity difference had the second largest rate of increase (slope $= 7.3 \times 10^{-5}$), and the ρv-component was the

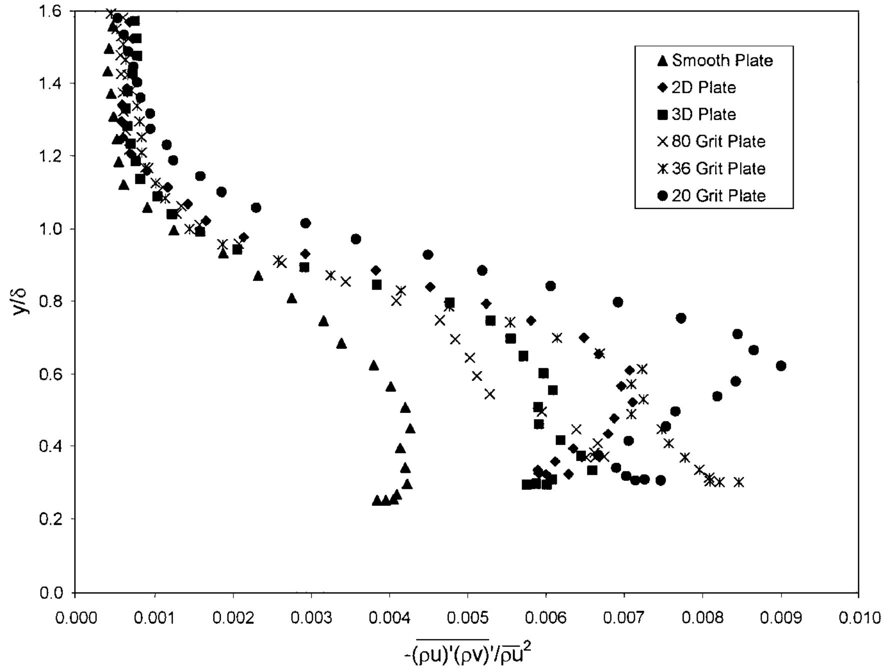

a) Outer-variable scaling

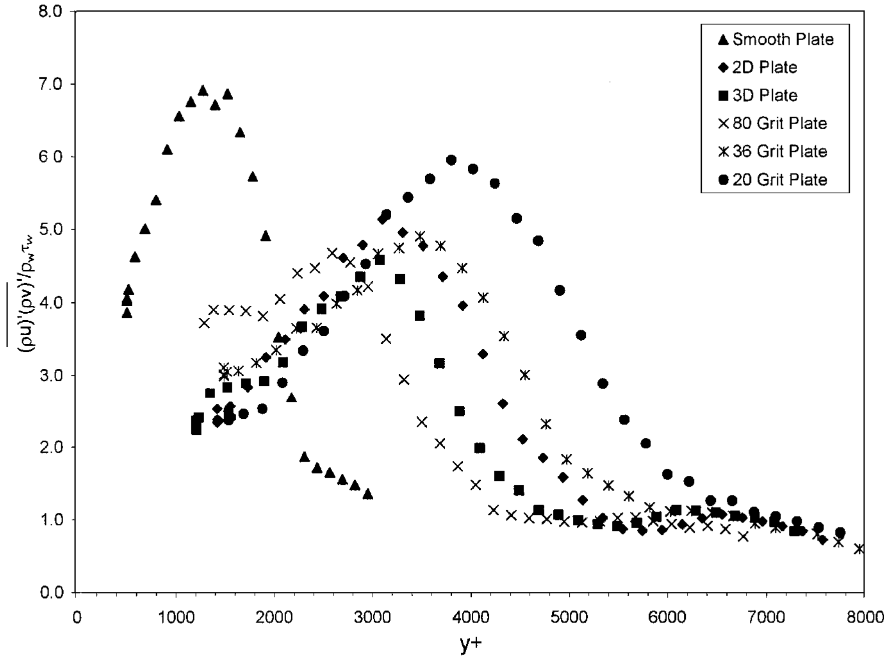

b) Inner-variable scaling

Fig. 11 The x–y component compressible Reynolds shear stress.

smallest (slope $= 5.6 \times 10^{-5}$). If the fluctuation magnitude is assumed to correspond to the eddy size, then the sand-grain trends indicated that increasing the roughness increased the lateral dimension of the eddies more than the axial or transverse dimensions.

The two-dimentional plate results in Fig. 9 were well above the sand-grain trend for both axial and spanwise components and were below the trend for the transverse component. Hence, the growth of the structures in the spanwise and axial direction was significantly greater than the sand-grain trend, which was consistent with structures that would be shed from cavities. The transverse dimension for the present two-dimensional geometry was smaller than that produced by a sand-grain plate with the same equivalent roughness height, which, coupled with the d-type flow, explains the smaller transverse fluctuations as compared with the sand-grain trend. The three-dimensional plate transverse and spanwise turbulence intensity values were well below the sand-grain trends. Considering that the three-dimensional plate roughness elements were relatively sparse as compared with the two-dimensional and sand-grain plates (i.e., 93.4% of the three-dimensional plate test surface was smooth), the smaller increase in the fluctuation levels was expected. Although significant differences between the machined and sand-grain results were discernible, the equivalent sand-grain roughness concept was a reasonable parameter to characterize the influence of roughness on the turbulence intensity levels for all six plates, where the results were all within approximately 10% of the trends shown in Fig. 9.

The kinematic Reynolds shear stress data are presented in Fig. 10. Smooth-plate laser Doppler velocimetry[21,22] and cross-film measurements[37] obtained in the same facility are included in Fig. 10a for comparison purposes. Excellent agreement between the present and previous studies was found.

The kinematic Reynolds shear stress data for each roughness model collapsed onto a single curve when scaled by the local mean streamwise velocity (Fig. 10a). As was the case for the velocity turbulence intensity data (Fig. 5), the two-dimensional plate shear stress data for $y/\delta < 0.4$ were lower in magnitude than those associated with the five other models. The agreement between the present rough-wall data and the incompressible results from Corrsin and Kistler,[8] without the compressibility transformation, was considered very good, considering the differences in flow conditions. The present smooth-plate kinematic Reynolds shear stress profiles reached a maximum value of approximately 2.0×10^{-3}, whereas the rough surface plates reached 7.7×10^{-3}, an increase of 285%.

The inner variable scaled results are shown in Figs. 10b and 10c. Plotting y^+ on either linear or logarithm scales did not collapse the data (Fig. 10b). Because the smooth-plate boundary-layer thickness and friction velocity were significantly lower, the smooth-plate data lay on a curve that was shifted toward smaller y^+ values. As was the case for the velocity turbulence intensities, the turbulent shear stress profiles (omitting the two-dimensional plate results) with inner variable scaling collapsed reasonably well when plotted vs y/δ (Fig. 10c).

The x–y plane fully compressible Reynolds shear stress [Eq. (2)] profiles, measured with the x–y plane cross-film probe, are shown in Fig. 11. Focusing first on the outer-scaled results (Fig. 11a), the compressible Reynolds shear stress did not collapse onto a single curve, as was the case for the kinematic Reynolds shear stresses (Fig. 5a). The compressible Reynolds shear stress for the smooth model reached a peak near $y/\delta \approx 0.3$–0.6. The rough-wall profiles were more complicated. First, the profiles reached a peak in the outer region near $y/\delta \approx 0.6$, and the magnitude of the peak was found to depend strongly on the equivalent roughness height. Second, a minimum (or a relatively sharp change in slope) in the profile was observed near $y/\delta \approx 0.4$, followed by an increase as the wall was approached. The compressible Reynolds shear stress levels with inner and mixed scaling (Figs. 11b and 11c) display similar trends as the axial turbulence intensities (Figs. 6b and 6c). Hence, those discussions are not repeated here.

The x–z plane compressible Reynolds shear stress also did not collapse when scaled with inner or outer variables. The results with outer variable scaling are shown in Fig. 12. Unlike the x–y data, the x–z plane values did not reach a peak over the distance measured but increased continuously with decreasing boundary-layer height.

The x–y and x–z compressible Reynolds shear stress peak differences relative to the smooth-plate peak scaled by the local mean streamwise mass flux for the five rough surface models vs roughness Reynolds number are shown in Fig. 13. The sand-grain roughness results for both components were nearly linear with k_s^+. The three-dimensional plate result agreed very well with the linear x–z component trend (slope $= 3.7 \times 10^{-5}$) established by the sand-grain plates. However, the two-dimensional model result was significantly (25%) above the trend, which indicated that the turbulent structures for the two-dimensional plate were more correlated in the x–z plane than was predicted by the trend. This result is consistent with the turbulence intensity data presented in Fig. 9. The x–y component sand-grain results also increased linearly, but at a much lower

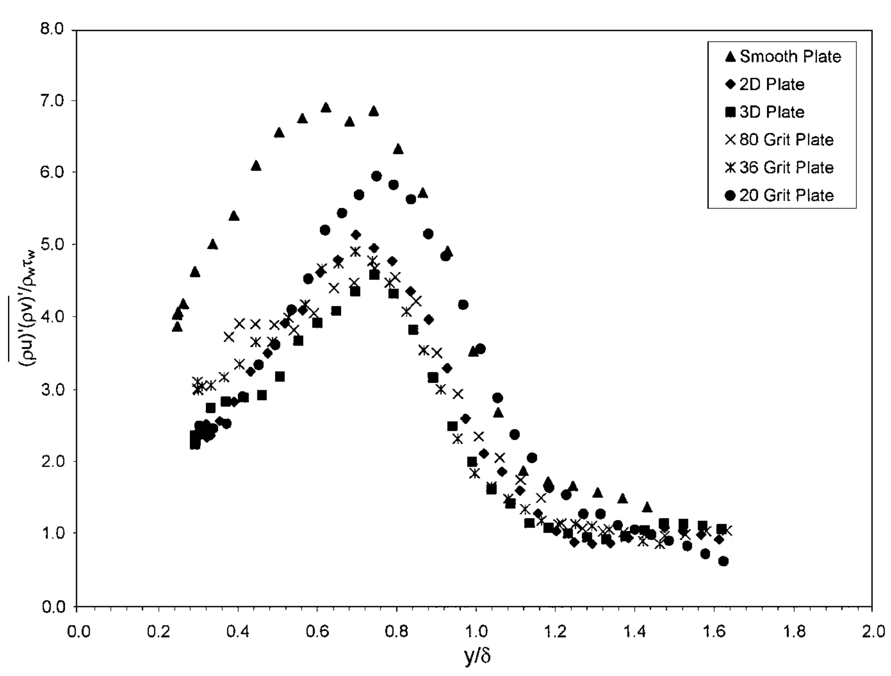

c) Mixed-variable scaling

Fig. 11 The x–y component compressible Reynolds shear stress (continued).

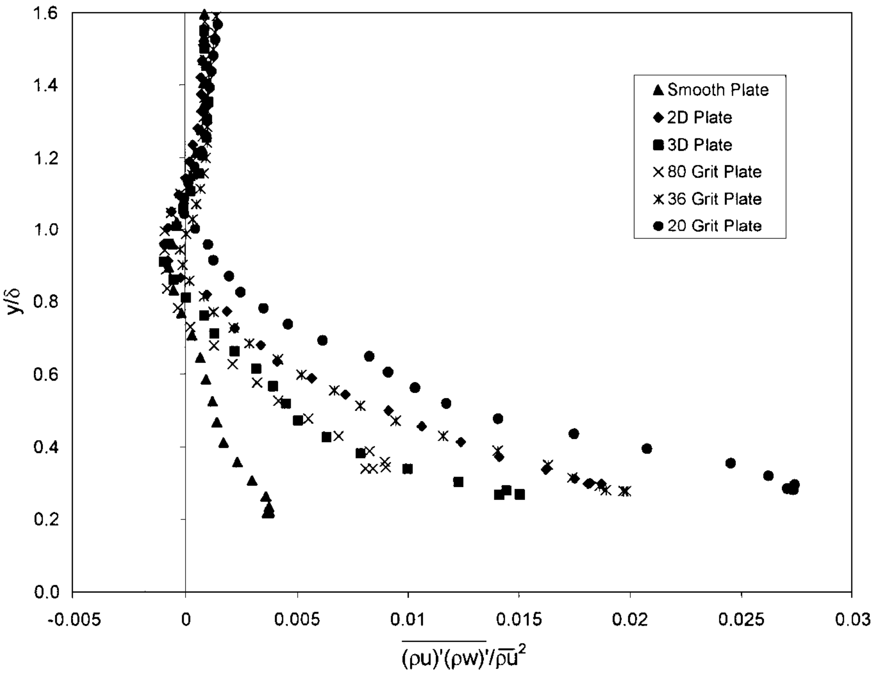

Fig. 12 The x–z component compressible Reynolds shear stress (outer-variable scaling).

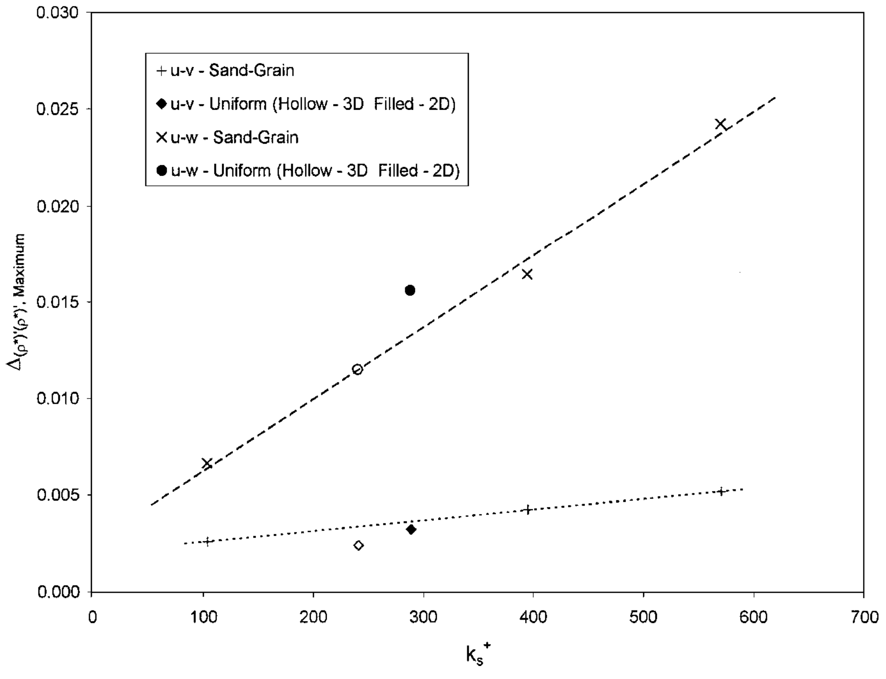

Fig. 13 Peak difference in the compressible Reynolds shear stress (outer scaling) vs k_s^+.

rate than the x–z component (x–y slope $= 5.6 \times 10^{-6}$). The three-dimensional plate result was well below (20%) the trend. Because 93.4% of the wall-surface area was smooth for the three-dimensional plate, the usual wall-damping effects[30] on the transverse fluctuation levels were expected.

Combining the cross-film and laser Doppler velocimetry measurements allowed for the estimation of correlation between the transverse velocity and density fluctuations,[23] i.e., $\overline{\rho' v'}/\overline{\rho u}$, which is equal to the negative of the Favre averaged velocity fluctuation $-\overline{v''}/\bar{U}$. Presented in Fig. 14a are the velocity-density correlation results with outer scaling. Since $\overline{\rho' v'}/\overline{\rho u}$ was a combination of the kinematic Reynolds and x–y compressible Reynolds shear stresses, and since the kinematic Reynolds shear stress profiles with outer scaling nearly collapsed for all of rough surfaces, data with outer scaling exhibited similar trends as the Reynolds shear stress data (Fig. 11a). Plotting the peak density-traverse-velocty correlation difference $\Delta_{\rho' v'}$, scaled by the local mean streamwise mass flux,[19] indicated that the rate of increase was approximately linear, and the slope was 8.0×10^{-6}. However, the scatter about the trend was nominally 12%. Hence, conclusions concerning the effects of roughness geometry were not discernible.

The transverse-velocity-density correlation with inner scaling is shown in Fig. 14b. Overall, the results strongly resemble the compressible Reynolds shear stress data shown in Fig. 11b. However, the nearer to the wall ($y^+ \approx 1000$–2500) velocity-correlation data did not collapse as well as the Reynolds shear stress data. The poor collapsing of the near-wall data is explained by recalling that the kinematic shear stress levels (Fig. 10a) did not collapse

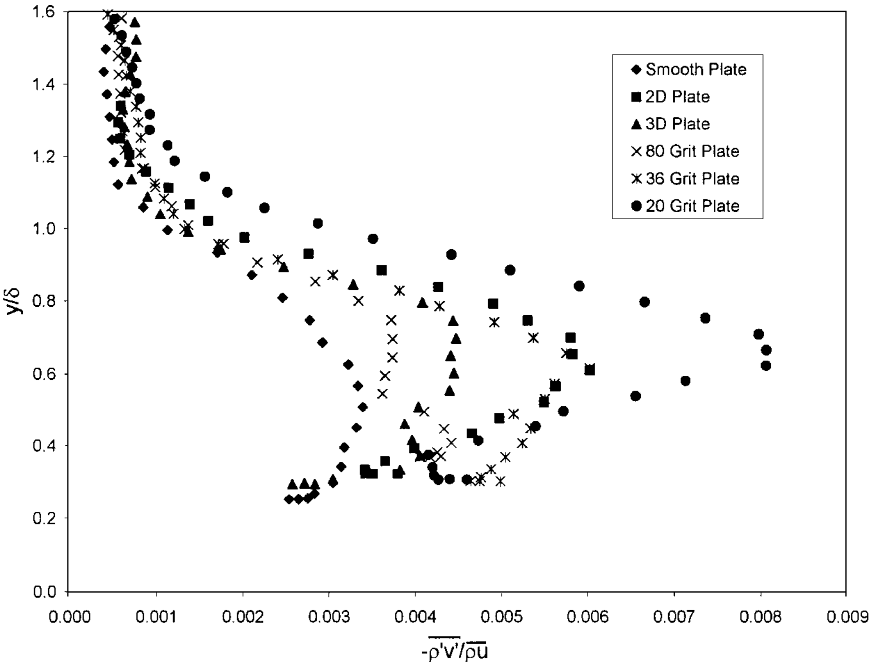

a) Outer-variable scaling

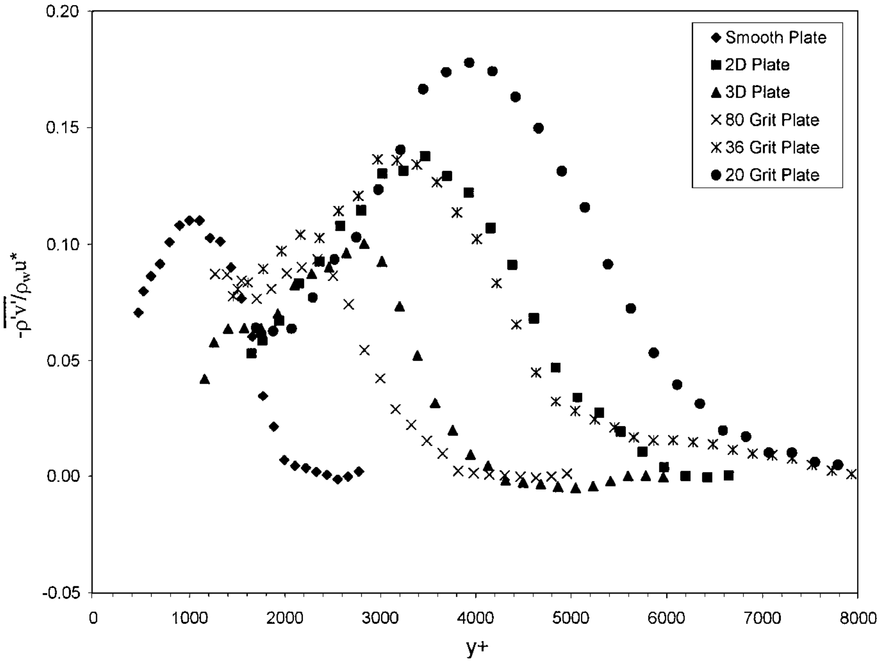

b) Inner-variable scaling

Fig. 14 Second order density-velocity correlation results.

in this region of the boundary layer, and using the strong Reynolds analogy[15] $[\overline{\rho' v'}/\overline{\rho u} = (\gamma - 1)M^2\overline{u'v'}/\bar{u}^2]$ to compare the relative magnitudes of the kinematic and compressible terms in the Reynolds shear stress. Away from the wall where the Mach number was relatively large, the velocity-density correlation was the dominant term the compressible Reynolds shear stress. For example, at $y/\delta = 0.7$, the mean Mach number for the rough plates was nominally 2.6, and the ratio of the second-to-first term in the Reynolds shear stress [i.e., on the right-hand side of Eq. (2)] was, based on the strong Reynolds analogy, 2.7. Closer to the wall, where the Mach number was small, the kinematic Reynolds shear stress term [first term on the right-hand side of Eq. (2)] became more important. At $y/\delta = 0.2$, the mean Mach number for the rough plates was nominally 1.4, and the ratio of the second-to-first term in the Reynolds shear stress was 0.8. Hence, it was not overly surprising that the data did not correlate as well closer to the wall.

Conclusions

An experimental study of the influence of surface roughness on the mean and turbulent flow properties of a high-speed ($M = 2.9$, $Re/\mathrm{m} = 2.0 \times 10^7$) turbulent boundary-layer flow was performed. Six wall topologies were tested: one smooth and five rough surfaces consisting of three random sand-grain plates ($k_s^+ = 100$, 400, and 570) and two uniformly machined plates ($k = 0.56$ mm for both). The experimental measurement techniques included a conventional pitot pressure probe, laser Doppler velocimetry, hot-wire anemometry, and color schlieren photography.

Mean flow measurements included detailed surveys of the velocity and density. The turbulent flow profiles included direct measurements of the kinematic velocity turbulence intensities, mass flux turbulence intensities, the kinematic Reynolds shear stress, the compressible Reynolds shear stress, and the density-velocity fluctuation correlation. In general, the results of this study describe the influence of roughness on the magnitude and scaling of the mean and turbulent statistical flow properties across the supersonic boundary layers. Eight specific conclusions are listed next.

1) The roughness elements were observed to protrude into the supersonic portion of the boundary layer, and the corresponding shock and expansion waves distorted the boundary edge and interacted with the boundary-layer turbulence.

2) The trends in the mean flow, observed for incompressible rough-wall flow, were found to hold for the present study when Van Driest II scaling was used.

3) In general, the rough-wall kinematic statistical turbulent flow properties measured with the laser Doppler velocimetry system collapsed on to a single curve when scaled with outer flow variables. The only exception was the two-dimensional plate, and it was expected that the turbulence production mechanisms associated with the d-type cavity were significantly different than for the remaining plates, which all had three-dimensional roughness patterns.

4) Roughness was found to extend the region of inner scaling applicability for the kinematic properties further out into the boundary layer.

5) Turbulent flow statistical properties with the explicit thermodynamic dependence did not collapse when scaled by local mean quantities, and increased almost linearly with k_s^+. Relative to the smooth-plate results, the (ρw) turbulence intensity component showed the largest rate increase with roughness, followed by the (ρu)- and then the (ρv)-component. In terms of second-order correlations, the x–z component of the full compressible Reynolds shear stress increased at the faster rate, followed by transverse-velocity-density correlation, and then the x–y component of the compressible Reynolds shear stress.

6) When scaled by inner flow variables, the rough-wall axial mass flux turbulence intensity, the x–y component of the compressible Reynolds shear stress, and the transverse component of the turbulent apparent mass flux data collapsed for the inner 70% of the boundary layer.

7) It was shown that the influence of smaller roughness elements increased the skin frictional losses more than the boundary-layer turbulence levels. However, as the roughness height was increased, the turbulence production relative to the frictional losses increased.

8) The equivalent sand-grain roughness was found to be an effective parameter to characterize the overall effects of roughness on the turbulent flow properties. The machined two-dimensional and three-dimensional plate results were in reasonable agreement with the sand-grain trends; however, significant variances (up to 25%) were observed and related back to roughness topology. Hence, it was concluded that the roughness topology was an important factor in the turbulence production.

Acknowledgments

The authors gratefully acknowledge Mark Glauser and Tom Beutner of the U.S. Air Force Office of Scientific Research and Diana Glawe and Mark Gruber of the U.S. Air Force Research Laboratory Propulsion Directorate for sponsoring this work. The authors also thank Tom Beutner for his insightful examination of the experimental data.

References

[1] Schlichting, H., "Boundary Layer Theory," *Mechanical Engineering*, McGraw–Hill, New York, 1955.

[2] Wilcox, D., *Turbulence Modeling for CFD*, DCW Industries, La Cañada, CA, 1993.

[3] Fernholz, I., Finley, M., and Mikulla, V., "A Futher Compilation of Compressible Boundary Layer Data with a Survey of Turbulence Data," AGARDograph 263, NATO, Technical Editing and Reproduction, London, Nov. 1981.

[4] Nikuradse, J., "Stromungsgesetze in Rauhen Rohren," *Forschung Arb. Ingenieurwesen*, No. 361, 1933.

[5] Simpson, R., "A Generalized Correlation of Roughness Density Effects on the Turbulent Boundary Layer," *AIAA Journal*, Vol. 11, No. 2, 1973, pp. 242–244.

[6] Antonia, R. A., and Wood, D. H., "Calculation of a Turbulent Boundary Layer Downstream of a Small Step Change in Surface Roughness," *Aeronautical Quarterly*, Vol. 26, Aug. 1975, pp. 202–210.

[7] Perry, A. E., Schofield, W. H., and Joubert, P. N., "Rough Wall Turbulent Boundary Layers," *Journal of Fluid Mechanics*, Vol. 37, 1969, pp. 383–413.

[8] Corrsin, S., and Kistler, A., "Free-Stream Boundaries of Turbulent Flow," NACA Rept. 1244, 1955.

[9] Dussuage, J.-P., Smith, R., Smits, A., Fernholtz, H., Finley, P., and Spina, E., "Turbulent Boundary Layers in Subsonic and Supersonic Flow," AGARDograph 335, NATO, Canada Communications Group, Hull, QC, Canada, July 1996.

[10] Goddard, F., "Effects of Uniformly Distributed Roughness on Turbulent Skin-Friction Drag at Supersonic Speeds," *Journal of Aero/Space Sciences*, Vol. 26, No. 1, 1959, pp. 1–24.

[11] Berg, D., "Surface Roughness Effect on a Mach 6 Turbulent Boundary Layer," *AIAA Journal*, Vol. 17, No. 9, 1979, pp. 929, 930.

[12] Reda, D., Ketter, F., and Fan, C., "Compressible Turbulent Skin Friction on Rough and Rough/Wavy Walls in Adiabatic Flow," *AIAA Journal*, Vol. 13, No. 5, 1975, pp. 553–555.

[13] Van Driest, E., "Turbulent Boundary Layers in Compressible Fluids," *Journal of Aeronautical Sciences*, Vol. 26, No. 3, 1951, pp. 287–319.

[14] Liepmann, H., and Goddard, F., "Note on Mach Number Effect upon the Skin Friction of Rough Surfaces," *Journal of Aero/Space Sciences*, Vol. 24, No. 10, 1957, pp. 784.

[15] Morkovin, M., "Effects of Compressibility on Turbulent Flows," *The Mechanics of Turbulence*, edited by A. Favre, Gordon and Breach, New York, 1961, pp. 368–380.

[16] Smits, A. J., Spina, E. F., Alving, A. E., Smith, R. W., Fernando, E. M., and Donovan, J. F., "A Comparison of the Turbulence Structure of Subsonic and Supersonic Boundary Layers," *Physics of Fluids*, A, Vol. 1, No. 11, 1989, pp. 1865–1875.

[17] Spina, E., Smits, A., and Robinson, S., "The Physics of Supersonic Turbulent Boundary Layers," *Annual Review of Fluid Mechanics*, Vol. 26, 1994, pp. 287–319.

[18] Smits, A., and Dussuage, J.-P., *Turbulent Shear Layers in Supersonic Flow*, American Inst. of Physics, Woodbury, NY, 1996.

[19] Latin, R. M., "The Influence of Surface Roughness on Supersonic High Reynolds Number Turbulent Boundary Layer Flow," Dept. of Aero/Astronautics, Air Force Inst. of Technology, Ph.D. Dissertation, AFIT/DS/ENY/98M-02, Wright–Patterson AFB, OH, April 1998.

[20] Hale, C., "Experimental Investigation of a Supersonic Turbulent Boundary Layer with Adverse Pressure Gradient," M.S. Thesis, Dept. of Aero/Astronautics, Air Force Inst. of Technology, AFIT/GAE/ENY/95D-12, Wright–Patterson AFB, OH, Dec. 1995.

[21] Luker, J., Hale, C., and Bowersox, R., "Experimental Characterization of the Turbulent Shear Stresses for Distorted Supersonic Boundary Layers," *Journal of Propulsion and Power*, Vol. 14, No. 1, 1998, pp. 110–118.

[22] Luker, J., Bowersox, R., and Buter, T., "Influence of a Curvature Driven Favorable Pressure Gradient on a Supersonic Turbulent Boundary Layer," *AIAA Journal*, In-Print, 1999.

[23] Bowersox, R., "Combined Laser Doppler Velocimetry and Cross-Wire Anemometry Analysis," *AIAA Journal*, Vol. 34, No. 11, 1996, pp. 2269–2275.

[24] Smith, D., and Smits, A., "A Study of the Effects of Curvature and Compression on the Behavior of a Supersonic Turbulent Boundary Layer," *Experiments in Fluids*, Vol. 18, 1995, pp. 363–369.

[25] Hazelton, D., Bowersox, R., Nuemann, D., and Hayes, J., "Skin Friction Measurements in a Mach 6 Inlet Test," AIAA Paper 97-2884, July 1997.

[26] Holman, J. P., *Experimental Methods for Engineers*, 3rd ed., McGraw–Hill, New York, 1978.

[27] Durst, F., Melling, A., and Whitelaw, J., *Principles and Practice of Laser-Doppler Anemometry*, Academic, New York, 1981.

[28] Adrian, R., "Laser Velocimetry," *Fluid Mechanics Measurements*, 2nd ed., edited by R. Goldstein, Taylor and Francis, Washington, DC, 1996, pp. 175–293.

[29] Christoph, G., and Fiore, A., "Numerical Simulation of Flow over Rough Surfaces, Including Effects of Shock Waves," Air Force Wright Labs., TR-83-3071, Wright–Patterson AFB, OH, Aug. 1983.

[30] Schetz, J., *Boundary Layer Analysis*, Prentice–Hall, Upper Saddle River, NJ, 1993.

[31] Hopkins, E., and Inouye, M., "An Evaluation of Theories for Predicting Turbulent Skin Friction and Heat Transfer on Plates at Supersonic and Hypersonic Mach Numbers," *AIAA Journal*, Vol. 9, No. 6, pp. 993–1003.

[32] White, F. M., *Viscous Fluid Flow*, 2nd edition, McGraw–Hill, New York, 1991.

[33] Hinze, O., *Turbulence*, McGraw–Hill, New York, 1975.

[34] Klebanoff, P. S., "Characteristics of Turbulence in a Boundary Layer with Zero Pressure Gradient," NACA Rept. 1247 (and NASA TN 3178), May 1954.

[35] Elena, M., and LaCharme, J.-P., "Experimental Study of a Supersonic Turbulent Boundary Layer Using a Laser Doppler Anemometer," *Journal of Theoretical and Applied Mechanics*, Vol. 7, No. 2, 1988, pp. 175–190.

[36] Heller, H., and Bliss, D., "Aerodynamically Induced Pressure Oscillations in Cavities: Physical Mechanisms and Suppression Concepts," Air Force Flight Dynamics Lab., AFFDL-TR-74-133, Wright–Patterson AFB, OH, Feb. 1975.

[37] Miller, R., Dotter, J., Bowersox, R., and Buter, T., "Measurements of Compressible Turbulence in a Supersonic Wall Bounded Flow with Pressure Gradient," *Joint ASME/JSME Fluids Engineering Conference*, FED-Vol. 224, American Society of Mechanical Engineers, New York, 1995, pp. 193–200.

M. Samimy
Associate Editor